Journal of Materials Chemistry A

PAPER

View Article Online
View Journal | View Issue

Cite this: J. Mater. Chem. A, 2015, 3, 12468

Received 26th March 2015
Accepted 6th May 2015

DOI: 10.1039/c5ta02201k

www.rsc.org/MaterialsA

Nanoscale MIL-101 supported RhNi nanoparticles: an efficient catalyst for hydrogen generation from hydrous hydrazine†

Pingping Zhao,[a] Nan Cao,[a] Wei Luo*[ab] and Gongzhen Cheng[a]

Nanoscale MIL-101 has been controlled, synthesized by a seeding method, and further used as the support for immobilizing RhNi nanoparticles (NPs) as efficient catalysts toward hydrogen generation from hydrous hydrazine in alkaline solution. Compared with other commercial materials and bulk MIL-101, RhNi NPs supported on nanoscale MIL-101 exhibit the highest catalytic activity and 100% hydrogen selectivity.

Introduction

Hydrogen has emerged as an attractive environmental-friendly alternative energy carrier to replace the CO_2-emitting C-containing fuels.[1] However, the search for safe and efficient hydrogen storage approaches is still the key obstacle to its widespread use, and thus numerous efforts have been made on such investigations.[2,3] Over the past decades, many approaches have been developed for searching for suitable hydrogen storage materials such as metal hydrides,[4] sorbent materials,[5] and chemical hydride systems.[6] Among them, the liquid-phase chemical hydrogen storage materials have been considered more advantageous over traditional solid-phase hydrogen storage materials due to their merits of using existing liquid-based fuel distribution, easy handling and transportation as well as the absence of any solid byproduct.[7] To this end, the liquid-phase hydrogen storage materials, such as formic acid (HCOOH),[8,9] liquid organic hydrogen carriers (LOHCs),[10] liquid amine borane complexes[6,11] and hydrous hydrazine,[12–16] have received considerable attention. Hydrous hydrazine ($N_2H_4 \cdot H_2O$) merits considerable attention as a potential candidate for chemical hydrogen storage material due to its high hydrogen content of 8.0 wt%, easy recharging through an electrolytic process and with nitrogen as the only byproduct *via* the reaction (eqn (1)).[17,18] However, in view of hydrogen storage application, the pathway of decomposition to ammonia by the reaction (eqn (2)) should be avoided.[19,20] Hence, a number of noble metal based nanocatalysts have been recently developed.[21,22]

$$N_2H_4 \rightarrow 2H_2 + N_2 \quad (1)$$

$$4N_2H_4 \rightarrow 2NH_3 + N_2 \quad (2)$$

For example, Xu's group first reported that Rh(0) NPs are highly active for the selective dehydrogenation of hydrous hydrazine, and it would be possible to achieve 100% conversion of hydrous hydrazine by alloying Ni to Rh.[12] To this end, numerous materials have been developed to disperse active metal NPs without aggregation and facilitate the electron transfer and mass transport kinetics during the catalytic reaction. Recently, Zhang's group reported graphene supported RhNi NPs with 100% H_2 selectivity and turnover frequency (TOF) value of 20 h^{-1} at room temperature.[23] Hur's group reported the hollow nickel-coated silica microspheres containing Rh NPs (Rh/Ni@SiO_2) with H_2 selectivity of 99.4% and TOF of 66 h^{-1}.[24] Thus, the development of new supported materials for RhNi nano-catalysts with high catalytic activity and 100% H_2 selectivity toward hydrogen generation from hydrazine is highly desirable for its practical application.

From another aspect, metal–organic frameworks (MOFs), as potential crystalline microporous materials, possessing the superiorities of extremely high porosity, large surface area, and chemical tunability, have been widely studied and applied.[25–29] Moreover, these materials can be scaled down to the nano-regime to afford the nanoscale MOFs (nMOFs), which have higher surface areas than their macroscopic counterparts. Thus, their applications in gas storage and separation, chemical sensors, drug delivery, and luminescence could be influenced.[30,31] Recently, carbonized nanoscaled MOFs has been reported as high performance electrocatalyst for oxygen reduction reaction or as an efficient heterogeneous catalyst for different oxidation reactions compared to their bulk MOFs.[32] However, loading metal NPs into the pores of nMOFs and then harvesting their catalytic performance has been rarely explored. Very recently, our group has reported that the bulk ZIF-8 supported RhNi NPs, $Rh_{34}Ni_{66}$@ZIF-8, exhibit a TOF value of 140 h^{-1} and 100% hydrogen selectivity at 50 °C;[33] however, due to the small pore size of ZIF-8, most of the RhNi NPs are located on

[a]College of Chemistry and Molecular Sciences, Wuhan University, Wuhan, Hubei 430072, P. R. China. E-mail: wluo@whu.edu.cn; Tel: +86 2768752366

[b]Suzhou Institute of Wuhan University, Suzhou, Jiangsu, 215123, P. R. China

† Electronic supplementary information (ESI) available. See DOI: 10.1039/c5ta02201k

the surface of ZIF-8. In this work, a new method toward size-controlled synthesis of nanoscale MOFs was proposed, and for the first time, the effects of supports with different dimensions toward the dehydrogenation of hydrous hydrazine were studied. MIL-101, which is a terephthalate-based Cr–MOF and is denoted as $Cr_3F(H_2O)_2][(O_2C)C_6H_4(CO_2)]_3\cdot nH_2O$ ($n \approx 25$), was selected as the support because of its large pore size, high thermal stability and high stability in water. As expected, RhNi NPs supported on nanoscale MIL-101 exhibit considerably higher catalytic activity than those supported on the bulk counterpart.

Experimental

Chemicals and materials

The chemical agents of $Cr(NO_3)_3\cdot 9H_2O$, $NiCl_2\cdot 6H_2O$, $RhCl_3\cdot 3H_2O$, HF, $HO_2CC_6H_4CO_2H$, $NaBH_4$, NH_4F and C_2H_5OH were commercially supported by Sinopharm Chemical Reagent Co., Ltd. $H_4N_2\cdot H_2O$ was provided by TCI Shanghai Co., Ltd. All of the agents were used without further purification. In our system, all solvent agents that were used consisted of ordinary distilled water.

Synthesis of MIL-101

2 mmol H_2BDC and 2 mmol $Cr(NO_3)_3\cdot 9H_2O$ were dissolved in 10 mL distilled water, and 1.5 mL hydrofluoric acid (3 wt%) was added into the mixture. After stirring, the aqueous solution was put into a 50 mL autoclave Teflon and then heated for 8 h at 200 °C. After washing by ethanol and centrifugation, the raw product of green powder was obtained. Then the green powder was soaked into the aqueous NH_4F solution overnight and followed by refluxing in ethanol for 12 h to obtain the purified MOF. The purified MIL-101 was further activated in vacuum at 150 °C overnight.

Nanoscale MIL-101 was synthesized with a similar method except that a trace amount of MIL-101 of different sizes was added into the Teflon-liner autoclave as a crystal nucleus before heating.

Synthesis of RhNi@MIL-101

To get the RhNi@MIL-101 catalysts with different Rh/Ni ratios (1 : 0; 1 : 4; 2 : 3; 3 : 2; 4 : 1; 0 : 1), 0.2 mmol metal ions with different compositions of Rh^{3+} and Ni^{2+} were added into 100 mg activated MIL-101 with distilled water added to maintain the volume at 10 mL. After stirring for 24 h, 37.8 mg $NaBH_4$ was added into the solution at 0 °C using an ice bath to maintain the temperature. The catalysts could be obtained by centrifugation, washing by ethanol and drying in the vacuum at 100 °C for 2 h.

RhNi NPs supported on different carriers were synthesized by a similar method except that γ-Al_2O_3, SiO_2, and carbon black were used as the supports.

Hydrous hydrazine decomposition reaction in aqueous solution

100 mg RhNi@MIL-101 catalyst and 80 mg NaOH solid was added into a two-neck bottle containing 4 mL water with magnetic stirring, one neck blocked by a rubber stopper and the other one connected with a pipe to release the gas. When the system remained stable, 0.1 mL hydrous hydrazine (98 wt%) was injected into the two-neck bottle and the record of gas release started. The gas released by hydrous hydrazine catalyzed by different catalysts was passed through a bottle containing 100 mL HCl solution (1 M) before being recorded. The temperature was controlled by a water bath. The extent of decomposition of hydrous hydrazine was calculated by eqn (3), and the turnover frequency value (TOF) was calculated by eqn (4).

$$X = (3\lambda - 1)/8 \ \lambda = n(H_2 + N_2)/n(H_2NNH_2) \quad (3)$$

$$\mathrm{TOF} = k_{H_2}\cdot n_{\mathrm{metal}}{}^{-1}\, n_{N_2H_4\cdot H_2O}{}^{-1}\, k_{H_2} = \mathrm{mol}_{H_2}\ h^{-1} \quad (4)$$

The hydrogen generation reaction was carried out at other temperatures (60, 70, 80 °C) to calculate the activation energy.

To demonstrate the effect of alkaline, the decomposition of hydrous hydrazine was carried out at different concentrations of NaOH solutions.

To demonstrate the effect of MOF, the decomposition was carried out using a similar method by the catalyzing of RhNi NPs supported on different carriers.

To test the durability, another 0.1 mL hydrous hydrazine (98 wt%) was added into the two-neck bottle after the previous decomposition completed.

Characterization

The metallic contents of Rh and Ni were determined by inductively coupled plasma-atomic emission spectroscopy (ICP-AES) (IRIS Intrepid II XSP, Thermo Fisher Scientific, USA). Powder X-ray diffraction (XRD) data scanned at 40 mA and 40 kV by a D8-Advance instrument (Bruker X-ray diffractometer PAN analytical X-ray system, German) using Cu Kα radiation source (λ = 0.154178 nm) at a velocity of 1° min^{-1} for the low-angle scanning and 6° min^{-1} for the wide-angle scanning. The characterization of BET surface data, which was based on N_2 adsorption/desorption isotherms at 77 K and controlled by liquid nitrogen, was measured using a Quantachrome NOVA 4200e. The morphologies and sizes of the samples were investigated by a transmission electron microscope (Tecnai G20 U-Twin, TEM) as well as an EDX detector (equipped with TEM) operated at an acceleration voltage of 200 kV. The XPS spectrum was measured by a Kratos XSAM 800 spectrophotometer. A gas analyzer (Ametek Dycor mass spectrometer) was used to obtain the MS spectrum of the gases released by the hydrous hydrazine, and they were collected under argon before being tested.

Results and discussion

The size-controlled synthesis of MIL-101 is illustrated in Scheme 1. Changing the ways of nucleation may strongly influence the morphologies and size of crystalline formed. Crystalline with sizes about 200 nm diameter would form without external crystal nuclei, as shown in Scheme 1a. Uniform crystals with nanomorphology and sizes of about 100 nm

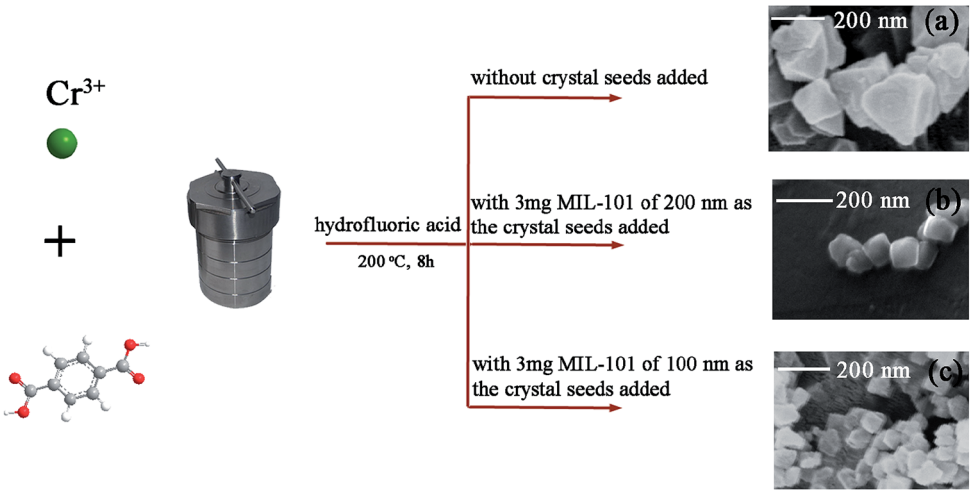

Scheme 1 Size-controlled synthesis of MIL-101.

diameter were obtained when trace amounts of 200 nm MIL-101 were added into the Teflon-liner autoclave as crystal nuclei (Scheme 1b), and nanoscale MIL-101 of 50 nm would form if trace amounts of 100 nm MIL-101 were added as the crystal nuclei before the heating treatment (Scheme 1c). Almost no differences of the peaks in low-angle powder X-ray diffraction pattern occurred between these MOFs with different dimensions (Fig. S1†), highly indicating that their structure remained consistent. The N_2 adsorption/desorption isotherms of three MOFs are shown in Fig. 1 and Table S1.† There are large differences of specific area, pore volume and pore size among these MOFs with different dimensions. As expected, the nMOFs exhibit considerably higher surface area and bigger pore volume and pore size than the bulk MIL-101. The 50 nm MIL-101 was further used as supports for RhNi NPs to catalyze the decomposition of hydrous hydrazine. The metal contents of Rh and Ni in the RhNi@MIL-101 catalyst were determined by inductively coupled plasma-atomic emission spectroscopy (ICP-AES) (Table 1). The low-angle PXRD profile ranging from 2° to 10° (Fig. 2A) showed no evident deficiency of the characteristic signals, which indicated that the intrinsic frameworks of MIL-101 kept well after the encapsulation of RhNi NPs. As shown in the wide-angle pattern of the PXRD profile in the 2θ range of 30°–70°, the dominant peak indexed to the plane of Rh (111) (PDF#05-0685) shifted toward wide angle when the Ni amount increased, which can be explained by the lattice compression effect of Ni and indicates that RhNi alloy is formed (Fig. 2B). Chemical shift of Rh $3d_{3/2}$ and Rh $3d_{5/2}$ at 311.7 and 307.0 eV, respectively, and the binding energies of Ni $2p_{1/2}$ and Ni $2p_{3/2}$ at 852.3 and 869.8 eV, respectively, in the X-ray photoelectron spectroscopy (XPS) were observed after etching treatment for 1000 s to remove the oxides on the surface, as shown in Fig. 3. The levels of Rh $3d_{3/2}$ and Rh $3d_{5/2}$ in the RhNi@MIL-101 nanocatalysts moved to higher binding energies relative to that for the pure-Rh, and the levels of Ni $2p_{1/2}$ and Ni $2p_{3/2}$ appeared shifted to lower energies relative to the monometallic Ni, highly indicating the alloy structure formed.[34] The spectrum for the $Rh_{58}Ni_{42}$@MIL-101 catalyst before etching treatment could be fitted with the oxidized formation of Ni 2p (856.3 and 874.5 eV) and Rh 3d (308.1 and 312.7 eV), which may be caused by the air

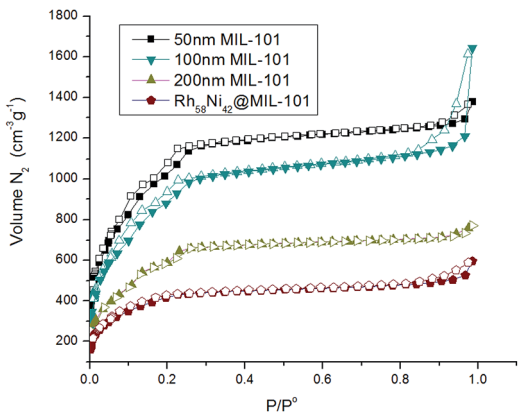

Fig. 1 N_2 sorption isotherms of different dimensions of MIL-101 and $Rh_{58}Ni_{42}$@MIL-101 at 77 K. Filled and open symbols represent adsorption and desorption branches, respectively.

Table 1 The Rh and Ni compositions determined by ICP-AES results

Catalyst	$Rh_{74}Ni_{26}$	$Rh_{58}Ni_{42}$	$Rh_{48}Ni_{52}$	$Rh_{34}Ni_{66}$	$Rh_{16}Ni_{84}$
Rh/Ni ratio of loading	$Rh_{80}Ni_{20}$	$Rh_{60}Ni_{40}$	$Rh_{50}Ni_{50}$	$Rh_{40}Ni_{60}$	$Rh_{20}Ni_{80}$
Ni (wt%)	1.5	2.84	3.38	5.27	7.3
Rh (wt%)	7.46	6.86	5.48	4.76	2.44
n(Rh + Ni)/Catalyst (mmol/100 mg)	0.098	0.115	0.111	0.136	0.148

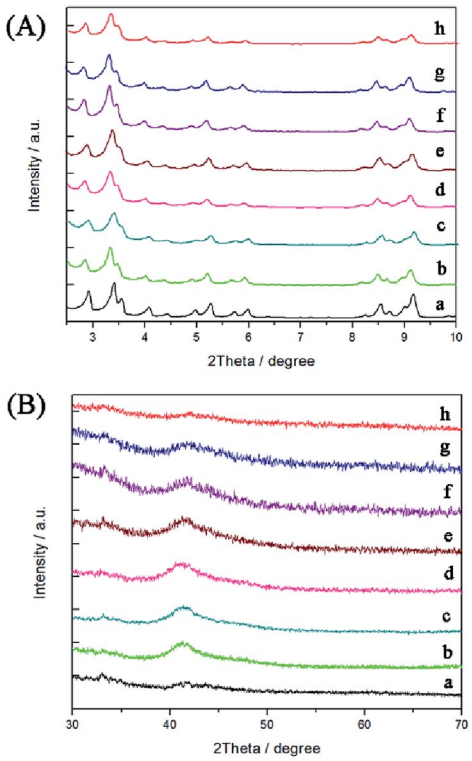

Fig. 2 (A and B) Low-angle and wide-angle Powder X-ray diffraction patterns of samples: (a) MIL-101; (b) Rh@MI-101; (c) $Rh_{74}Ni_{26}$@MIL-101; (d) $Rh_{58}Ni_{42}$@MIL-101; (e) $Rh_{48}Ni_{52}$@MIL-101; (f) $Rh_{34}Ni_{66}$@MIL-101; (g) $Rh_{16}Ni_{84}$@MIL-101; (h) Ni@MIL-101.

during the sample preparation. No signals of B were observed from the XPS spectrum, and the binding energies of Cr 2p (576.6 eV, 587.3 eV) strongly demonstrated the Cr–O bonding formation in the catalysts (Fig. S2†). Based on the XPS analysis, no evident interaction between the RhNi NPs and the MOFs existed. However, the synergistic effect between RhNi NPs and MIL-101 was suggested, which originated from the host-guest cooperation between nanoparticles and MOF, and the limited window size of MIL-101 prevent RhNi NPs from crossing the cavities and thus minimizes the possibility of aggregation of RhNi NPs. The magnetic effect of RhNi NPs disappeared after immobilization on the pores of MIL-101, as shown in Fig. S3,† which is due to the encapsulation effect of MOF. Furthermore, the distributions of elements from the area mapping showed a uniform distribution of the metallic distribution of Ni, Rh and Cr in the $Rh_{58}Ni_{42}$@MIL-101 catalysts, which highly indicated that the alloy structure of RhNi NPs is formed (Fig. 4).

Transmission electron microscopic image (TEM) of the $Rh_{58}Ni_{42}$@MIL-101 along with energy-dispersive X-ray spectroscopy (EDX) measurements analysis exhibited well-dispersed RhNi NPs with an average diameter of 1.9 nm (Fig. 5). Due to the large pore size, limited window size and hybrid pore surface of MIL-101, uniform RhNi NPs were formed with size and shape controlled. These NPs were small enough to be encapsulated into the two mesoporous cavities of MIL-101 (2.9 and 3.4 nm) and big enough to be confined in the pores of the framework by the windows of MIL-101 (1.2 and 1.6 nm), and thus they enhanced the H_2 selectivity and activity as well as the durability for dehydrogenation of hydrous hydrazine (*vide infra*). In addition, the specific area, pore volume and pore size of MIL-101 significantly

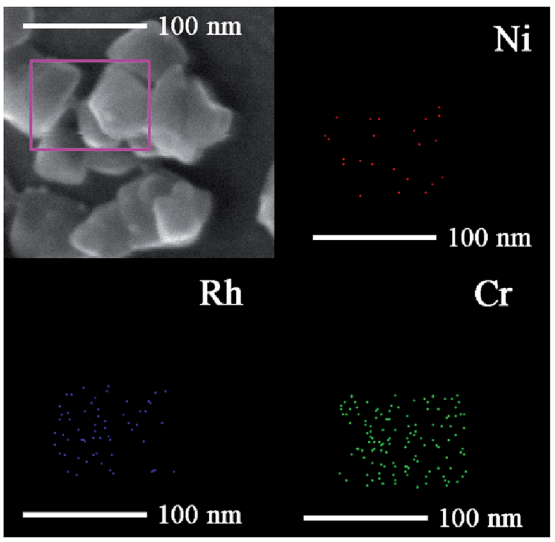

Fig. 4 SEM of the $Rh_{58}Ni_{42}$@MIL-101 and the distributions of Ni, Rh and Cr.

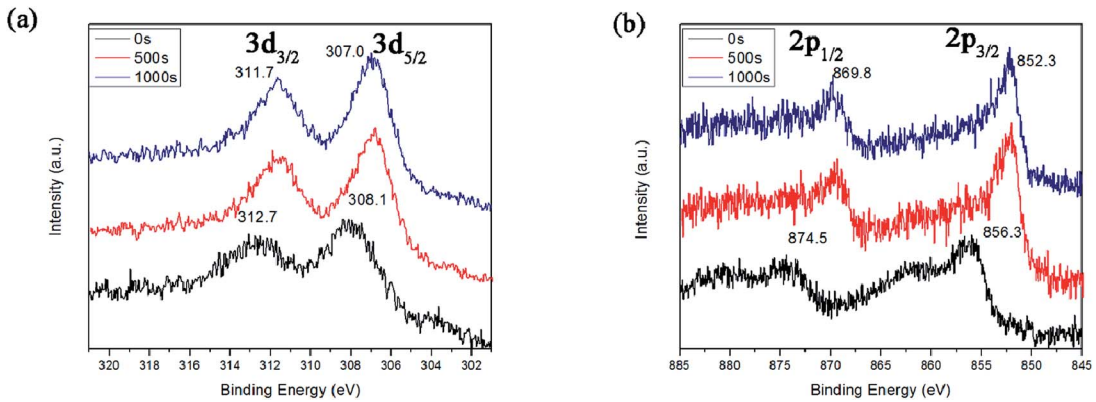

Fig. 3 XPS spectra of Rh 3d (a) and Ni 2p (b) for catalyst $Rh_{58}Ni_{42}$@MIL-101 with different etch time.

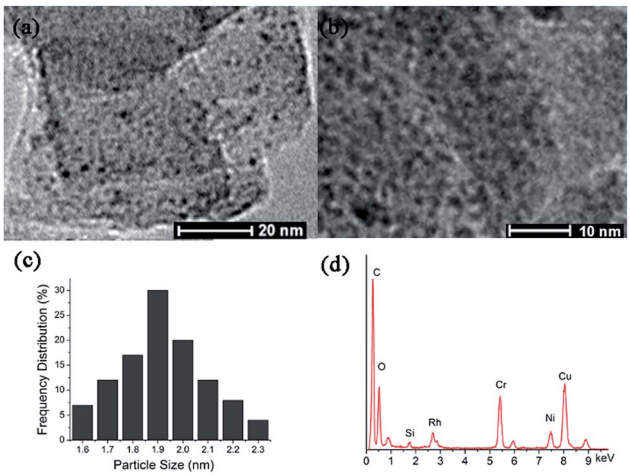

Fig. 5 (a and b) TEM images of $Rh_{58}Ni_{42}$@MIL-101 with different magnifications. (c) Particle size distributions of $Rh_{58}Ni_{42}$ NPs; (d) EDX of $Rh_{58}Ni_{42}$@MIL-101.

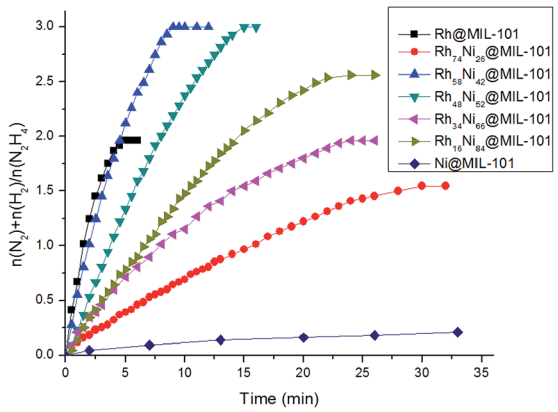

Fig. 6 Time course plots for the decomposition of hydrous hydrazine over $Rh_{58}Ni_{42}$@MIL-101 with NaOH (0.5 M) at 50 °C (catalyst = 0.100 g; $N_2H_4 \cdot H_2O$ = 0.1 mL).

decreased after RhNi NPs encapsulation (Fig. 1, Table S1†), indicating that the cavities of MIL-101 were either occupied by the well dispersed RhNi NPs or blocked by the RhNi NPs.[35]

The activity of RhNi@MIL-101 catalysts with various compositions of RhNi NPs toward the dehydrogenation of hydrous hydrazine was investigated in alkaline solution (0.5 M NaOH) at 50 °C (Fig. 6). The hydrogen selectivity and activity were strongly dependent on the composition of the Rh/Ni ratio. Ni@MIL-101 was almost catalytically inactive towards the decomposition of hydrous hydrazine; Rh@MIL-101 showed the highest TOF value (478 h^{-1}) but poor selectivity of H_2 generation (only 65%). Considering the hydrogen selectivity and generation rate, $Rh_{58}Ni_{42}$@MIL-101 exhibits the best catalytic activity, with 100% hydrogen selectivity and TOF value of 344 h^{-1} at 50 °C. The comparisons of this work and other similar catalytic systems toward the dehydrogenation of hydrous hydrazine are listed in Table 2. Moreover, the catalytic activity of the mixture of Ni@MIL-101 and Rh@MIL-101 was studied (Fig. 7b). Only 1.27 equiv. gas with 42.3% hydrogen selectivity was released during more than one hour, strongly indicating the synergistic effect of Rh and Ni in molecular-scale induces the enhancement of catalytic activity and hydrogen selectivity (Scheme S1†). This might be explained by the Sabatier principle, which states that optimal catalytic activity could be achieved by altering the surface of catalysts.[38] As Ni has a smaller lattice constant than Rh, alloying Ni would increase the compression of the RhNi alloy and the binding energy toward reactive intermediates. However, large amounts of Ni would occupy the available surface sites and poison the catalyst. Furthermore, the mass spectroscopy of the gas released over $Rh_{58}Ni_{42}$@MIL-101 further indicates the 100% H_2 selectivity (Fig. S4†).

To study the effects of the supported materials on the catalytic performances toward the dehydrogenation of alkaline solution of hydrous hydrazine, catalysts were prepared by loading RhNi NPs on other carriers such as γ-Al_2O_3, SiO_2 and carbon black. Moreover, the catalytic performance of a physical mixture of RhNi with MIL-101 toward the dehydrogenation of hydrous hydrazine was tested. All the catalysts tested were inferior to that of $Rh_{58}Ni_{42}$@MIL-101 (Fig. 7a). RhNi/C showed

Table 2 Comparison of the decompositions of hydrazine monohydrate catalyzed by catalysts in this study and previous reports

Catalyst	T (°C)	H_2 selectivity/%	TOF[a] (h^{-1})	Reference
NiFe	70	100	6.6	3
$Rh_{58}Ni_{42}$@MIL-101	50	100	344	This study
$Ni_{66}Rh_{34}$@ZIF-8	50	100	140	33
$Ni_{64.1}Mo_{11.5}B_{24.4}$-$La(OH)_3$	50	100	13.3	15
$NiIr_{0.059}/Al_2O_3$	30	99	12.4	13
$NiPt_{0.057}/Al_2O_3$	30	98	16.5	18
$Ni_{0.9}Pt_{0.1}/Ce_2O_3$	25	100	76	22
Co–B nanospheres	25	21.3	77.9	36
Rh_4Ni	25	100	9.6	12
9.86 wt% Fe–B/MWCNTs	25	97	878	20
Co–B–N–H nanowires	20	100	912	37
Ni_3Fe/C	20	100	555.6	14

[a] The TOF values were calculated according to the original data provided by the reports.

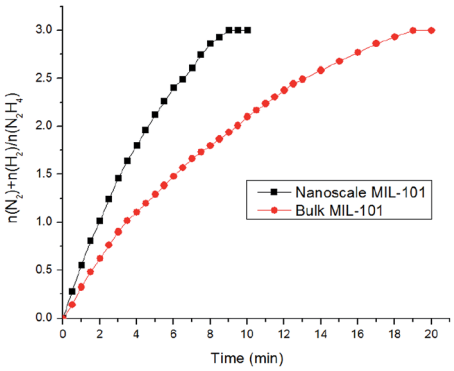

Fig. 7 Time plots of $Rh_{58}Ni_{42}$ NPs catalytic dehydrogenation of hydrous hydrazine in the presence of NaOH (0.5 M) at 50 °C: with different size MIL-101 as the supports.

that a higher activity but lower hydrogen selectivity toward the dehydrogenation of hydrous hydrazine is due to the fact that both of the two decomposed pathways occurred, which was further confirmed by the MS profile (Fig. S5†). In the RhNi NPs or physical mixture of RhNi NPs and MIL-101, only 2.56 equiv. gas with 85.3% hydrogen selectivity were released for more than 30 min, highlighting the synergistic effect between nanoscale MIL-101 and RhNi NPs as a key factor of RhNi@MIL-101 in promoting the decomposition of hydrous hydrazine. The TEM of RhNi NPs without supports exhibited a serious aggregation, as shown in Fig. S6,† which is the major reason for decrease in the catalytic activities of RhNi NPs.

The effects of MOFs with different nano-dimensions toward the dehydrogenation of hydrous hydrazine were further tested. As expected, RhNi NPs supported on nanoscale MIL-101 exhibit considerably higher catalytic performance (Fig. 8), indicating that nano-morphology catalysts, which possess higher surface area, could provide higher dispersion and more catalytic sites in solution in comparison to its bulk counterpart.

To study the effect of pH, the dehydrogenation of hydrous hydrazine with different concentrations of NaOH were investigated (Fig. 9). The catalytic activity and hydrogen selectivity were highly dependent on the alkaline concentration, and the dehydrogenation of hydrous hydrazine showed the best activity in 0.5 M NaOH solution. In the absence of NaOH, the catalytic activity and hydrogen selectivity decreased significantly, which may be caused by the acceleration of the rate-determining step of hydrazine decomposition ($N_2H_4 \rightarrow N_2H_3^* + H^*$) and suppresses the formation of basic NH_3 by NaOH.[35]

In addition, the catalytic reactions of the dehydrogenation of hydrous hydrazine catalyzed by $Rh_{58}Ni_{42}$@MIL-101 were carried out at various temperatures from 50 °C to 80 °C to obtain the Arrhenius activation energy (E_a) (Fig. 10a). The values of rate constant k at different temperatures were calculated from the slope of the linear part of each plot. From the Arrhenius plot of ln k *vs.* $1/T$ for the catalyst, E_a was determined to be 33 kJ mol^{-1} (Fig. 10b).

The reusability of $Rh_{58}Ni_{42}$@MIL-101 was tested by successively adding the same amount of hydrous hydrazine after the completion of the previous run at 50 °C. High activity and 100% hydrogen selectivity still remained after 5 cycles (Fig. 11). From the SEM and PXRD pattern in Fig. S7,† there is no change of the as-synthesized catalyst after 5 run tests. However, the TEM result indicates that some big particles exist after the reusability test, which may be the reason for the decrease in BET surface area. Further work on enhancement of the stability of the catalysts is still underway.

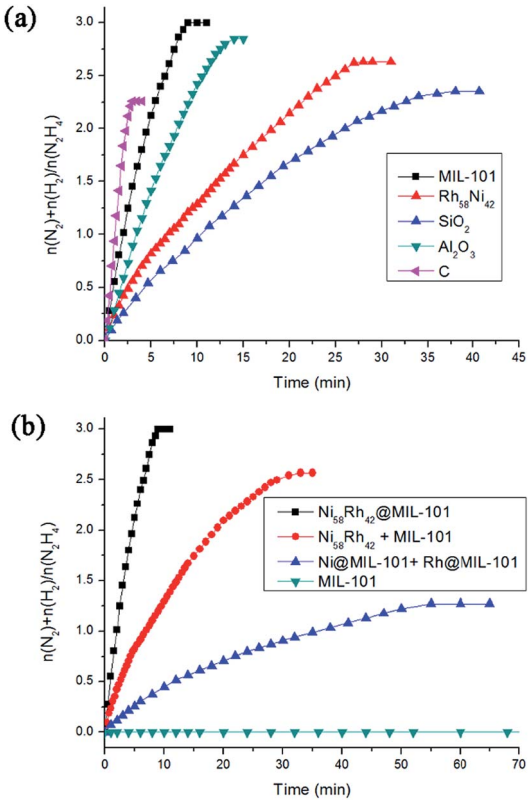

Fig. 8 Time plots of catalytic dehydrogenation of hydrous hydrazine in the presence of NaOH (0.5 M) at 50 °C: (a) by $Rh_{58}Ni_{42}$ NPs with different supported materials; (b) by $Rh_{58}Ni_{42}$@MIL-101, a physical mixture of $Rh_{58}Ni_{42}$ with MIL-101, and Ni@MIL-101 and Rh@MIL-101.

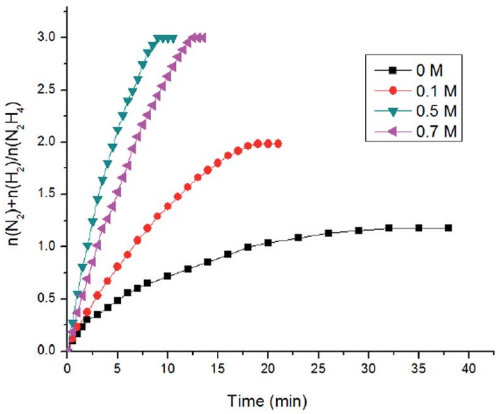

Fig. 9 Time course plots for the decomposition of hydrous hydrazine over $Rh_{58}Ni_{42}$@MIL-101 in alkaline solution with different concentrations of NaOH at 50 °C.

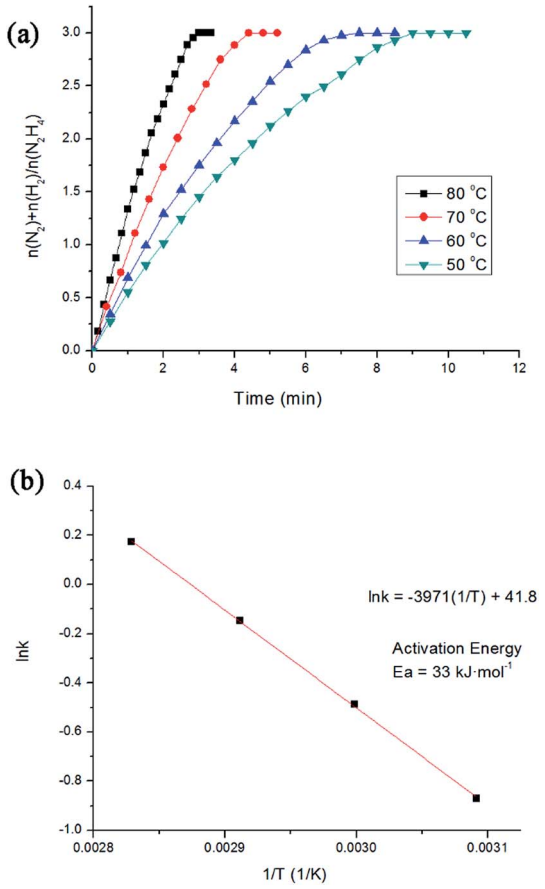

Fig. 10 (a) Time course plots for hydrogen generation by the decomposition of hydrous hydrazine by $Rh_{58}Ni_{42}$@MIL-101 at, 50 °C, 60 °C, 70 °C and 80 °C. (b) Plot of ln *k versus* 1/T during the hydrous hydrazine decomposition over $Rh_{58}Ni_{42}$@MIL-101 at different temperatures.

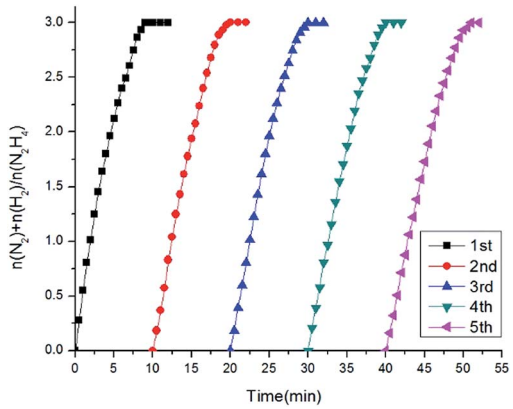

Fig. 11 Durability test of $Rh_{58}Ni_{42}$@MIL-101 for the decomposition of hydrous hydrazine in aqueous NaOH solution (0.5 M) at 50 °C (catalyst = 0.100 g; $N_2H_4 \cdot H_2O$ = 0.1 mL).

Conclusions

In summary, nanoscale MIL-101 was synthesized by changing the way of crystalline nucleation by a simple method of adding trace amounts of crystal nuclei. Due to the nano-morphology, higher surface areas and higher dispersion in solution, RhNi NPs supported on nanoscale MIL-101 exhibit the highest catalytic activity compared with the bulk MIL-101 and other commercial supported materials toward hydrogen generation from hydrazine in alkaline solution. The development of nanoscale MOFs as support to anchor active metal NPs and thus harvesting their catalytic activity may open up a new avenue for preparing other nMOFs supported NPs for more applications.

Acknowledgements

This work was financially supported by the National Natural Science Foundation of China (21201134), the Natural Science Foundation of Jiangsu Province (BK20130370), the Natural Science Foundation of Hubei Province (2013CFB288), the Creative Research Groups of Hubei Province (2014CFA007) and Large-scale Instrument and Equipment Sharing Foundation of Wuhan University.

Notes and references

1 M. G. Schultz, T. Diehl, G. P. Brasseur and W. Zittel, *Science*, 2003, **302**, 624–627.
2 L. Schlapbach and A. Züttel, *Nature*, 2001, **414**, 353–358.
3 S. K. Singh, A. K. Singh, K. Aranishi and Q. Xu, *J. Am. Chem. Soc.*, 2011, **133**, 19638–19641.
4 J. Graetz, *Chem. Soc. Rev.*, 2009, **38**, 73–82.
5 M. P. Suh, H. J. Park, T. K. Prasad and D.-W. Lim, *Chem. Rev.*, 2012, **112**, 782–835.
6 W. Luo, P. G. Campbell, L. N. Zakharov and S.-Y. Liu, *J. Am. Chem. Soc.*, 2011, **133**, 19326–19329.
7 A. W. van den Berg and C. O. Areán, *Chem. Commun.*, 2008, 668–681.
8 K. Tedsree, T. Li, S. Jones, C. W. A. Chan, K. M. K. Yu, P. A. Bagot, E. A. Marquis, G. D. Smith and S. C. E. Tsang, *Nat. Nanotechnol.*, 2011, **6**, 302–307.
9 H. Dai, N. Cao, L. Yang, J. Su and G. Cheng, *J. Mater. Chem. A*, 2014, **2**, 11060–11064.
10 N. Brückner, K. Obesser, A. Bösmann, D. Teichmann, W. Arlt, J. Dungs and P. Wasserscheid, *ChemSusChem*, 2014, **7**, 229–235.
11 D. Tong, X. Zeng, W. Chu, D. Wang and P. Wu, *J. Mater. Sci.*, 2010, **45**, 2862–2867.
12 S. K. Singh and Q. Xu, *J. Am. Chem. Soc.*, 2009, **131**, 18032–18033.
13 L. He, Y. Huang, X. Y. Liu, L. Li, A. Wang, X. Wang, C.-Y. Mou and T. Zhang, *Appl. Catal., B*, 2014, **147**, 779–788.
14 D. G. Tong, D. M. Tang, W. Chu, G. F. Gu and P. Wu, *J. Mater. Chem. A*, 2013, **1**, 6425–6432.
15 J. Zhang, Q. Kang, Z. Yang, H. Dai, D. Zhuang and P. Wang, *J. Mater. Chem. A*, 2013, **1**, 11623–11628.
16 S. Y. Fu, Y. Z. Li, W. Chu, C. Li and D. G. Tong, *Catal. Sci. Technol.*, 2015, **5**, 1638–1649.
17 N. Cao, L. Yang, C. Du, J. Su, W. Luo and G. Cheng, *J. Mater. Chem. A*, 2014, **2**, 14344–14347.

18 L. He, Y. Huang, A. Wang, Y. Liu, X. Liu, X. Chen, J. J. Delgado, X. Wang and T. Zhang, *J. Catal.*, 2013, **298**, 1–9.
19 N. Cao, L. Yang, H. Dai, T. Liu, J. Su, X. Wu, W. Luo and G. Cheng, *Inorg. Chem.*, 2014, **53**, 10122–10128.
20 D. G. Tong, W. Chu, P. Wu, G. F. Gu and L. Zhang, *J. Mater. Chem. A*, 2013, **1**, 358–366.
21 L. He, Y. Huang, A. Wang, X. Wang, X. Chen, J. J. Delgado and T. Zhang, *Angew. Chem.*, 2012, **124**, 6295–6298.
22 H.-L. Wang, J.-M. Yan, Z.-L. Wang, O. Song-Il and Q. Jiang, *J. Mater. Chem. A*, 2013, **1**, 14957–14962.
23 J. Wang, X.-B. Zhang, Z.-L. Wang, L.-M. Wang and Y. Zhang, *Energy Environ. Sci.*, 2012, **5**, 6885–6888.
24 J. B. Yoo, H. S. Kim, S. H. Kang, B. Lee and N. H. Hur, *J. Mater. Chem. A*, 2014, **2**, 18929–18937.
25 A. Aijaz and Q. Xu, *J. Phys. Chem. Lett.*, 2014, **5**, 1400–1411.
26 Q.-L. Zhu and Q. Xu, *Chem. Soc. Rev.*, 2014, **43**, 5468–5512.
27 B. P. Biswal, D. B. Shinde, V. K. Pillai and R. Banerjee, *Nanoscale*, 2013, **5**, 10556–10561.
28 T. Pham, K. A. Forrest, R. Banerjee, G. Orcajo, J. Eckert and B. Space, *J. Phys. Chem. C*, 2015, **119**, 1078–1090.
29 J. Thote, H. B. Aiyappa, A. Deshpande, D. Díaz Díaz, S. Kurungot and R. Banerjee, *Chem.–Eur. J.*, 2014, **20**, 15961–15965.
30 A. Carné, C. Carbonell, I. Imaz and D. Maspoch, *Chem. Soc. Rev.*, 2011, **40**, 291–305.
31 J. Della Rocca, D. Liu and W. Lin, *Acc. Chem. Res.*, 2011, **44**, 957–968.
32 S. Zhao, H. Yin, L. Du, L. He, K. Zhao, L. Chang, G. Yin, H. Zhao, S. Liu and Z. Tang, *ACS Nano*, 2014, **8**, 12660–12668.
33 B. Xia, N. Cao, H. Dai, J. Su, X. Wu, W. Luo and G. Cheng, *ChemCatChem*, 2014, **6**, 2549–2552.
34 S. K. Singh and Q. Xu, *Chem. Commun.*, 2010, **46**, 6545–6547.
35 X. Gu, Z.-H. Lu, H.-L. Jiang, T. Akita and Q. Xu, *J. Am. Chem. Soc.*, 2011, **133**, 11822–11825.
36 D. G. Tong, W. Chu, P. Wu and L. Zhang, *RSC Adv.*, 2012, **2**, 2369–2376.
37 F. Yang, Y. Z. Li, W. Chu, C. Li and D. G. Tong, *Catal. Sci. Technol.*, 2014, **4**, 3168–3179.
38 J. Greeley, T. F. Jaramillo, J. Bonde, I. Chorkendorff and J. K. Nørskov, *Nat. Mater.*, 2006, **5**, 909–913.